Magnetic Force Microscopy Characterization of Magnetic Nanowires and Nanotubes

5

Muhammad Ramzan Tabasum, Fatih Zighem, Luc Piraux, and Bernard Nysten

Contents

1 Definition of the Topic

Magnetic force microscopy (MFM) is one of the operational modes of atomic force microscopy (AFM). In this mode, a magnetic probe is brought close to the sample surface and interacts with the magnetic stray fields emanating from the sample. The strength of the local magnetostatic interaction determines the vertical motion of the tip as it scans across the sample. Since early 1990s, it has been widely used in

M.R. Tabasum (✉) • L. Piraux • B. Nysten
Institute of Condensed Matter and Nanosciences, Bio and Soft Matter (IMCN/BSMA), Université catholique de Louvain, Louvain La Neuve, Belgium
e-mail: muhammad.tabasum@uclouvain.be; ramzan.x.tabasum@gsk.com; luc.piraux@uclouvain.be; bernard.nysten@uclouvain.be

F. Zighem
LSPM, CNRS-Université Paris 13, Sorbonne Paris Cité, Villetaneuse, France
e-mail: zighem@gmail.com

C.S.S.R. Kumar (ed.), *Magnetic Characterization Techniques for Nanomaterials*,
DOI 10.1007/978-3-662-52780-1_5

fundamental research on magnetic materials, as well as in the development of magnetic recording components. It has the capacity to map the local stray fields emanating from individual magnetic nanostructures of the sample, hence providing insight into its magnetic behavior.

2 Overview

The fundamental properties of 2D arrays of magnetic nanowires and nanotubes (NWs and NTs) have been well described theoretically, but real systems are subject to certain flaws and imperfections which strongly affect the mechanism and dynamics of magnetization reversal. Therefore, before exploiting the vast potential of magnetic NWs and NTs, there is a need to investigate the materials parameters as well as the field dependent magnetic properties in real systems.

Amongst the various issues at stake for a comprehensive understanding of these arrays is the influence of long-range dipolar interactions because these interactions strongly influence the magnetization reversal and thus the switching field distributions (SFD) which plays a significant role for information storage. Particularly, the width of the SFD is important since smaller values of this parameter leads to less recording errors and it is also a measure of the quality of the recording media. Consequently, the understanding and evaluation of the distinct parameters influencing the interactions and the intrinsic SFD in the magnetization reversal process of such arrays is critical for the development of magnetic recording media. It is shown that the intrinsic SFD mostly originates from nonuniformities of the geometrical parameters such as the aspect ratio and the shape of the magnetic nanostructures.

This chapter provides an overview of the MFM characterization studies undertaken to understand the reversal behavior of 2D arrays of magnetic NWs and NTs at the nanoscale and the motivations to investigate isolated single domain NWs and NTs.

3 Introduction

The area of materials science and physics dealing with the magnetic properties of objects having at least one dimension in the nanoscopic range, from 1 to 100 nm, is called *nanomagnetism*. Its scope includes the study of the properties and applications of magnetic nanoparticles, nanodots, nanowires, thin films and multilayers, and also macroscopic samples containing nanoscopic particles [1].

Nanomaterials are of great interest because they exhibit valuable and unique physical and chemical properties. Furthermore, there is an increasing demand for new types of materials with different structures and improved physical properties to be used in miniaturized devices. This has led, along with other conceivable candidates, to the production of magnetic NWs and NTs because of their unique magnetic properties and potential technological applications in, for instance, microwave devices [2–4], chemical sensors [5, 6], high-density data storage [7–9], and light emitters [10–12]. Magnetic NWs and NTs are attractive in physics, but they also got

an enormous attraction in biological and biomedical applications [13–16]. They have been proven to be promising tool for cell manipulation and positioning and have also been suggested for hyperthermia usage to treat cancer cells [17]. In this application, heating is caused by the magnetic hysteresis and is used to destroy harmful cells. To overcome the limitation of superparamagnetism in existing magnetic recording media and to achieve high storage densities, single domain magnetic NWs fabricated into the holes of porous membranes [7, 18] have been found very attractive because of the large shape anisotropy *that may favor patterned media* with *perpendicular anisotropy suitable for* high-density magnetic storage. Suitable separation between the nanowires is needed to avoid undesired effects due to interwire interaction and magnetic dipolar coupling. There are numerous ways to grow NWs and NTs of various kinds and materials but electrodeposition is considered to be the most versatile and low-cost technique [19].

Generally, magnetization curves, obtained from magnetometry instruments such as SQUID, AGFM, and VSM, are used to characterize the behavior of nanostructured magnetic materials [16, 20–27]. The characteristic features of these curves are linked to the type of material, size, and shape of the entity, orientation of the sample with respect to the field and sample magnetization history. Nevertheless, such global information is not sufficient for a complete comprehension of magnetic interactions and switching of individual particles at the nanoscale. Therefore when it comes to nanomagnetic characterization, new cutting edge tools should be proposed.

The huge progress in nanotechnology would have not been possible without the modern trend towards the miniaturization of devices and the development of specific instrumentation, e.g., atomic force microscope (AFM) that can visualize nanomaterials [28]. Magnetic force microscopy (MFM), a special mode of operation of AFM, employs a magnetic probe (including the tip) to characterize magnetic materials. Compared with the other magnetometry instruments, MFM has the capacity to map the local stray fields emanating from individual nanostructures, hence providing insight into their magnetic behavior. MFM presents a sufficient resolution to simultaneously provide information about the topography and the static magnetic configuration of individual magnetic nanostructures [29–34]. This technique can be used not only as a characterization instrument but also for magnetic reading and writing of individual nanostructures [30].

Switching field distribution (SFD), along with saturation magnetization, remanent magnetization, and coercive and saturation fields, is a key parameter to describe the magnetic behavior of magnetic units. Switching field is strongly dependent on geometric parameters and on the magnetization of surrounding neighbors. In very dense arrays of NWs, the width of the SFD is due to external effects like dipolar interactions and to intrinsic factors such as inhomogeneity of the diameters. However, the relative importance of both phenomena was not clear. Therefore MFM has been widely employed to explore the properties of magnetic NWs (SFD, coercivity, and remanent magnetization) in dense arrays as well as in dilute ones [7, 8, 35–37].

After having addressed the methods to fabricate NWs/NTs and the experimental set-up to use MFM, this chapter reviews the salient research works presented by other groups during the past few years to grasp the phenomena of magnetization reversal in

2D arrays of interacting magnetic NWs and NTs. Then, our most recent works to determine the magnetization reversal progress in low-density two-dimensional arrays of ferromagnetic NWs and NTs are presented. In these arrays, the NWs are sufficiently isolated from each other to neglect the dipolar interactions between them. This helps to avoid the difficult corrections which are necessary for dense NWs arrays, leading to an easier analysis and interpretation of the MFM experiments.

4 Experimental and Instrumental Methodology

4.1 Materials

4.1.1 Alumina and Track Etched Polymer Templates

A template, in general, is a predesigned structure within which a network exists for further utilization. Formation of porous as well as barrier-like alumina films by aluminum anodization is a well-known procedure which has been studied since 1950s [38] and forms the base of generating highly ordered alumina templates [39] with nonintersecting and uniform pore channels (anodized aluminum oxide membranes or AAO membranes). This type of template has been widely used for the fabrication and study of high-density arrays of NWs and NTs [7–9, 40, 41].

In order to directly obtain the intrinsic properties of magnetic NWs by MFM, analyses should be realized on arrays of noninteracting isolated NWs which cannot be obtained using the AAO membranes due to the high pore density. This has been recently performed, thanks to the use of polymer track-etched membranes, in which pore density can be controlled, as templates for the synthesis of the magnetic NWs. The creation of pores in a polymer film is a two-step process, namely, a) irradiation with heavy ions and b) chemical etching of the ion track to produce randomly distributed pores. This process allows controlling the size, shape, and density of pores over a wide range of values. Indeed, sizes of 10 nm to several micrometers, with a length to diameter ratio between 10 and 1000 are possible, and the pore density can range from 10^5 to 10^{11} cm^{-2} [42, 43].

4.1.2 Electrodeposition of NWs and NTs

There are various strategies, depending upon the applications, for embedding the matter of interest within the pores of templates. Electrodeposition of metals into the pores of nanoporous membranes is particularly attractive [44] because: (a) it is a simple, low-cost, high-throughput technique for fabricating large arrays of nanowires with monodispersed diameter and length; (b) it provides the ability to tailor the size, length, shape, and morphology of the material deposited by controlling the template morphology and the synthesis parameters; and (c) it provides the ability to introduce composition modulation along the wire length, which in turn enables precise control on architecture and magnetic properties.

Before starting the process of deposition, a thin conductive layer of Au or Cu is sputtered on one side of the membrane which served as cathode during the subsequent electrochemical deposition of the metal in the nanopores. The template is first

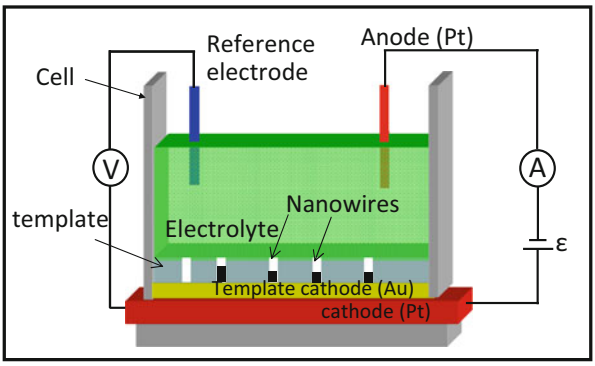

Fig. 5.1 Schematic representation of the electrodeposition cell containing the nanoporous template in contact with the cathode and filled with an electrolyte

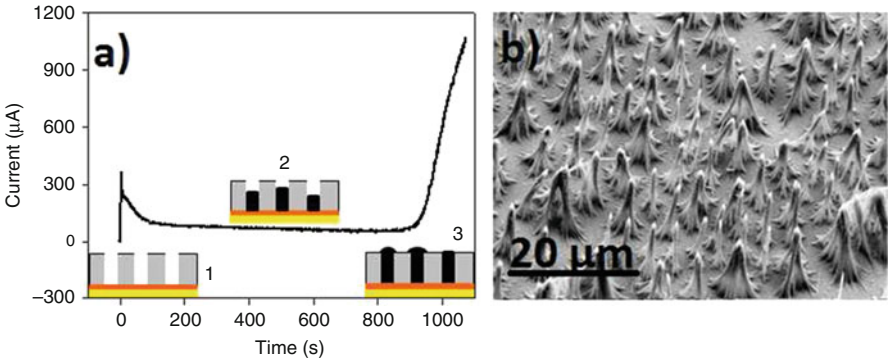

Fig. 5.2 (**a**) Current as a function of time corresponding to the electrodeposition of an array of $Ni_{80}Fe_{20}$ NWs in potentiostatic mode at a potential of −1.05 V. Different stages are indicated with numbers. (**b**) Assemblies of the deposited wires after PC dissolution

attached to the cathode of the electrolytic cell and then brought in contact with the deposition solution in which a Pt anode and a reference electrode are dipped later. In our experiments, electrodeposition of NW arrays is carried out in a Teflon cell using an EG&G Princeton Applied Research potentiostat model 263. Figure 5.1 illustrates the common setup.

The electrodeposition is initiated by the application of a potential bias between the cathode and the anode. When an electric field is applied, cations diffuse toward and reduce at the cathode, resulting in the growth of nanowires inside the pores of the template. The nanowires grow inside the pores of the membrane from the cathode because the electrolyte is confined to the exposed side of the membrane. During the electrodeposition, the voltage is generally kept constant and its value depends on the metal or alloy to be deposited. The evolution of the current between the anode and the cathode is used to measure the progress of the nanowires growth. The current passing between the anode and the cathode depends on the effective area of each of those electrodes. The three stages of this process can be identified in the evolution of the current with time (Fig. 5.2).

Table 5.1 Electrolytic solutions and potentials used to grow Ni, NiFe, and CoFe NWs. The composition of the solutions is given in g/l and the pH is maintained at 3.8 for all the solutions

Solution	$NiSO_4$	$FeSO_4$	$CoSO_4$	H_3BO_3	E (V)
Ni	262.8	–	–	20.3	−1.1
$Ni_{80}Fe_{20}$	131.4	5.5	–	24.7	−1
$Co_{55}Fe_{45}$	–	40	80	30	−0.9

The Stage 1 corresponds to the nucleation and the germination of the species to be deposited in the virgin template. It is characterized by the sudden increase of the current which is due to the difference between the equilibrium potential of the ions in solution and the applied potential. The growth of the wires inside the pores (Stage 2) is characterized by an approximately constant current. The ion concentration is equilibrated and the surface of the deposit is simply the sum of the areas of the pores. The constant current value in this stage depends on the pore size and density. When the deposit reaches the surface of the membrane, the current increases rapidly (Stage 3) because the pores are filled and the metal begins to deposit as caps at the end of the wires. The electrodeposition is stopped just before the Stage 3 to avoid overgrowth out of the membrane. Figure 5.2b shows typical electrodeposited wires released from a PC membrane.

For the fabrication of the dilute NW arrays in PC templates, different electrolytes based on Co, Ni, and Fe sulfates have been employed. In addition to these sulfates, each solution contained boric acid (H_3BO_3) which served as pH buffering agent and improved the electric conduction, avoiding parasite reductions at the cathode like the hydrogen ions reduction ($2H^+ + 2e^- \rightarrow H_2(g)$). This chemical reaction modifies the solution pH, which has significant influence on the morphology of the deposited material. Boric acid ensures a stable solution pH. However, if a specific solution pH is desired, the pH can be controlled by adding sulfuric acid (H_2SO_4) or sodium hydroxide (NaOH).

Apart from the deposition of pure materials, the electrodeposition method offers the possibility of depositing alloys of two or even more different ionic species (e.g., $Ni_{80}Fe_{20}$). The compositions of the solutions used to deposit different metallic nanowires of Ni, $Ni_{80}Fe_{20}$, and $Co_{55}Fe_{45}$ are shown in Table 5.1. The details of the fabrication of Ni, $Ni_{80}Fe_{20}$, and $Co_{55}Fe_{45}$ NWs can be found in references [34, 37].

In NTs not only the diameter and length but also the wall thickness can be tuned. Electrodeposition may be used as a fabrication methodology, but it is not as straight forward as for fabricating NWs. Therefore, modified routes of electrodeposition and various other approaches have been used to grow NTs of pure metals and alloys [40, 45–53]

Arrays of Ni NTs were fabricated in track-etched 21 μm thick PC membranes with pore diameter (*D*) of 150 nm and packing density (*P*) of 6 %. They were fabricated using a two-step procedure as depicted in Fig. 5.3a. The process starts by growing Ni/Cu core/shell NWs at a constant potential of −1.0 V using a 0.4 M $Ni(H_2NSO_3)\bullet 4H_2O$, 0.05 M $CuSO_4\bullet 5H_2O$, and 0.1 M H_3BO_3 electrolyte. The Cu core is later electrochemically etched at a potential of + 0.2 V [47, 54].

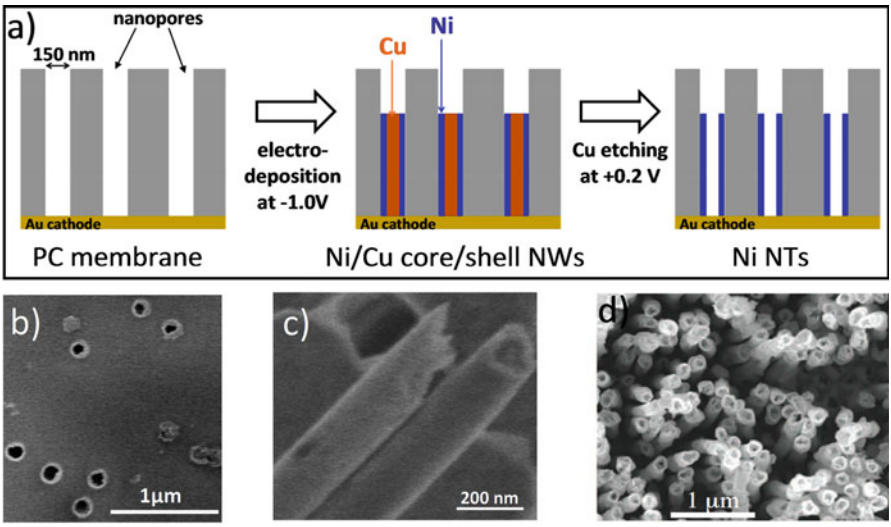

Fig. 5.3 (**a**) Sketch of the NTs fabrication process presenting the two different steps. (**b**) SEM images of Ni NTs in the PC membrane after etching the metal cathode (**c**) of two Ni NTs after the dissolution of the PC membrane and (**d**) of a large number of NTs obtained with a higher-packing-density membrane ($P = 10$ %). Reprinted with permission from [34] All rights reserved, © IOP Publishing

4.1.3 Packing Density and Interwire Distance

The nanowires packing factor is defined as the product of the wire density per unit surface (n) by the cross-sectional area of a single wire (S) and can be written as:

$$P = n \, . \, S$$

By counting the number of the wires of known diameter in a given MFM image, the packing density can be easily calculated using the above formula. For instance, the packing density of the sample in Fig. 5.4a is around $P \approx 0.15$ %. However sometimes depending upon the diameter of the nanopores, the packing density (P) may be quite different from the pore density (P_{pores}). It has been shown that the packing density in PC can be drastically low when the pore sizes is less than 20 nm [43], which is not the case in our samples as verified by SEM and shown in Fig. 5.4b.

SEM and MFM images can thus be used to calculate the packing density as well as the mean interwire distance (I_D). To calculate I_D, the distance between a selected wire and its nearest neighbors is measured as depicted in Fig. 5.5. Since PC membranes have random distribution of track etched pores, the procedure is repeated for several wires on the same image to get the average interwire distance. For instance, calculations done at various spots of the image presented in Fig. 5.5 gave an average I_D around 1000 nm.

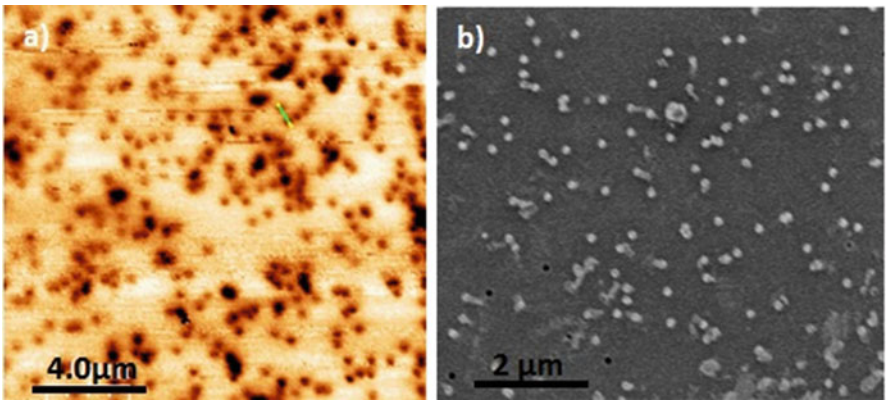

Fig. 5.4 (**a**) MFM image of NWs of 50 nm and 0.15 % packing density. (**b**) SEM micrograph of 150 nm NWs array showing that the pore density is almost the same as packing density

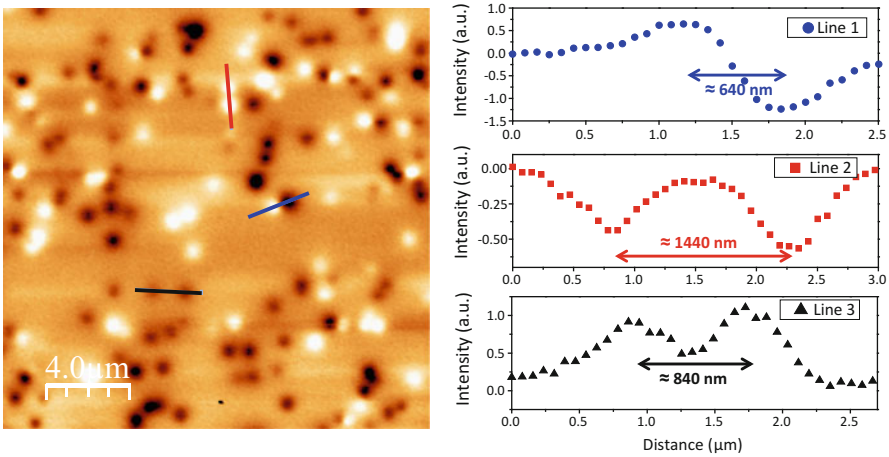

Fig. 5.5 MFM image showing the chosen wire and line to measure the interwire distance with one of its neighbors (*left*). The vertical axis of the graphs represents the signal strength whereas the horizontal axis represents the distance between the two signal peaks, i.e., between two wires (*right*)

4.1.4 Sample Preparation for MFM Measurements

As it has been stated in Sect. 2.1.2, the electrodeposition is stopped before the NWs (or NTs) start growing out of the template and forms interconnected wires as caps. Nevertheless, since all the wires do not breed at a uniform rate, the top surface of the PC-template was not used for MFM characterization. After electrodeposition, the gold and chromium layers were removed by chemical etching in order to obtain a smooth surface where all the nanowires tips at that side of the PC membrane are close to the surface (Fig. 5.6). The metallic cathode was first removed by dipping the sample into a 100 g/l KI + 25 g/l I_2 solution to etch the gold layer. The remaining Cr

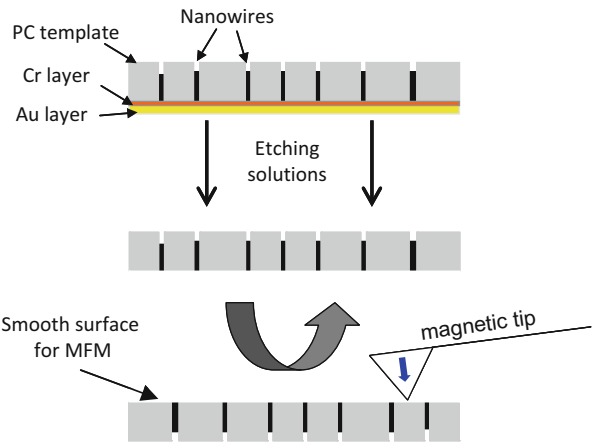

Fig. 5.6 Sample preparation for MFM measurements

layer was etched using a Cr etching solution composed of 52 g $KMNO_4$ in 600 ml of 5 M NaOH in H_2O. This step is very crucial since the Cr etching solution, containing NaOH, can also etch the PC membrane [55]. This phenomenon has indeed been observed (Fig. 5.7). It has also been demonstrated that longer etching time leads to rougher surfaces with nanorods sticking out of the surface (Fig. 5.7). It is thus recommended to use short etching times for the Cr layer, less than half an hour.

Using this procedure, the extremity of the nanowires can be imaged while keeping them into the template, as well as their magnetic state: "up" or "down" for positive or negative magnetized nanowires, respectively, if we consider a uniform magnetization inside the nanowires. The surface prepared by this procedure can also be used to characterize the sample using SEM so that one can verify the growth of the nanowires inside the holes.

4.2 MFM Experiments

4.2.1 Setup for MFM Measurements

This paragraph briefly presents the MFM setup allowing experiments in presence of an applied magnetic field parallel to the NWs (or NTs) axis. The schematic of the modified setup is depicted in Fig. 5.8. An adapted electromagnet was used which has the capacity to apply around 5 kOe magnetic field at maximum. This limit was satisfactory for most of the samples studied in the low-density samples. For high-density samples, various groups have developed strategies to apply external magnetic field during the measurements (see the references in Sect. 3.1). The electromagnet was made of a steel breech containing 800 turns of copper wire of dimensions 2 $\times$ 1 mm. The diameter of the breech is 13 cm and the assembly is 71 mm in height with a total weight of $\sim$6 kg. The dimensions have been chosen keeping in view the hosting room available in "Agilent" AFM.

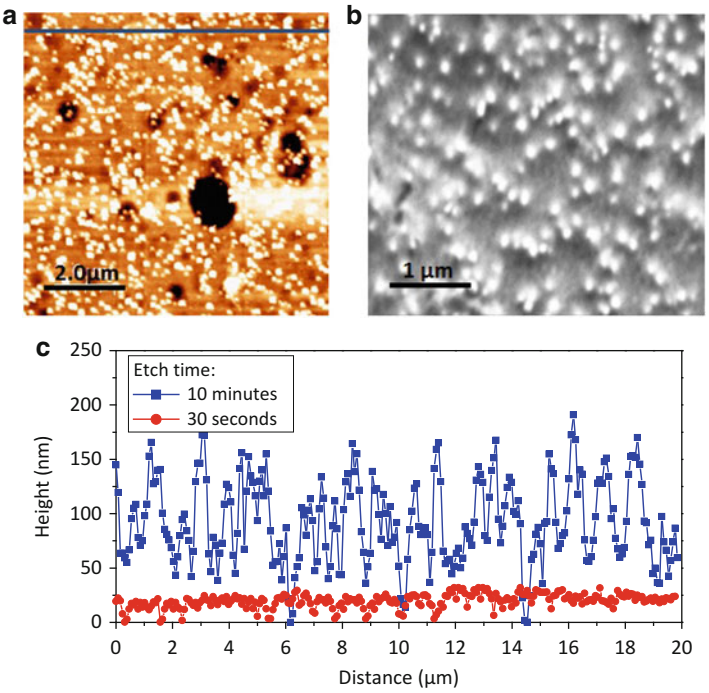

Fig. 5.7 (**a**, **b**) Topography as measured by MFM and SEM after etching the cathode layer. (**c**) Effect of etching time on the topography details which correspond to the *dark gray horizontal line* on *top* of (**a**)

The analyses were realized in amplitude-modulation (AM-AFM) using a double pass procedure. First, the topography of one line was recorded in standard intermittent-contact mode. Then, the probe was lifted up a few tens of nanometers (typically 60 nm) and the same line was scanned at constant probe-surface distance; the phase signal proportional to the magnetic interaction gradient was simultaneously recorded. The details of working principle and modes of operations of MFM have been presented in [29, 56, 57].

Thanks to this setup, in situ or in-field measurements can be performed:

> *In situ* MFM images correspond to measurements performed at zero applied field after applying an *in situ* external magnetic field parallel to the NWs (or NTs) axis (Fig. 5.9). This means that the applied magnetic field is switched off during the measurements.
>
> *In field* MFM images correspond to measurements performed in the presence of a static magnetic field applied in the direction of the NWs (or NTs) axis. So, in this "mode", the applied magnetic field is not switched off during the image recording.

However, it should be noted that in situ and in-field MFM images give the same results when studying arrays of low packing density. Indeed, in this case, as a consequence of the weak dipolar interactions between nanowires, measurements

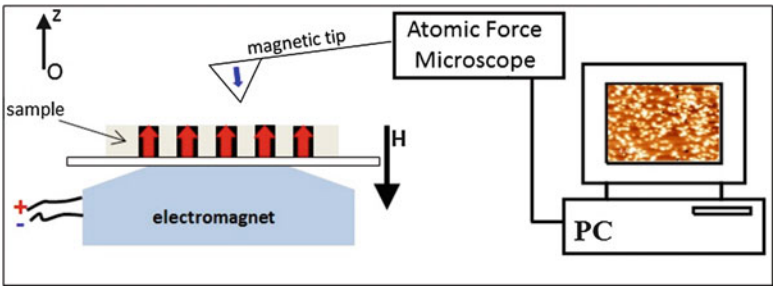

Fig. 5.8 Schematic of the MFM setup

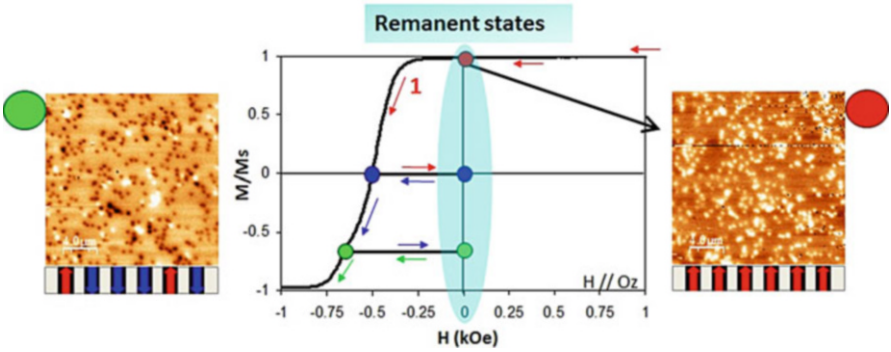

Fig. 5.9 Showing the in situ MFM images recorded at remanent states when the sample is saturated (*right*) and when almost 75 % of the wires have been switched (*left*). The example was performed in an array of low packing density (<1 %) where the dipolar interactions are too weak to significantly play a role in the magnetization reversal of the array

done without switching off the applied field H_0 and at zero fields after applying H_0 are close to each other (this is presented and discussed later for some arrays: see Fig. 5.25). That was the reason why low-packing-density samples are most of the time characterized in the remanent states.

4.2.2 Magnetization Curves and Switching Field Distribution Measured by MFM

A typical study of a low-packing-density array of NWs is presented in Figs. 5.9 and 5.10. Prior to the measurements the sample is saturated along the NWs axis. The tip is magnetized in the opposite direction of the magnetization of the sample. This leads to a white (attractive) contrast. Then, a series of magnetic fields along the magnetization of the tip but opposite to the sample's initial saturation field are applied.

As depicted in Fig. 5.10, counting the number of NWs which reversed their magnetization direction after each increment of applied field give access to the switching field distribution (SFD). MFM-magnetization curves can be obtained by using the following formula:

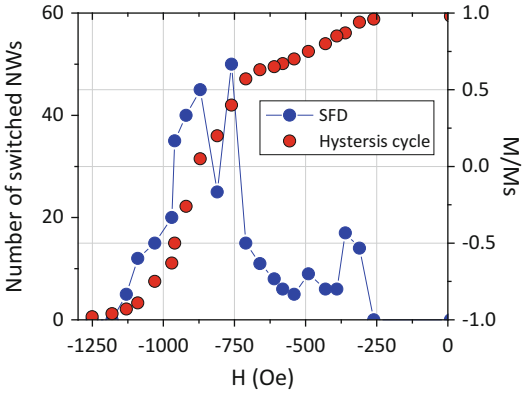

Fig. 5.10 Switching field distribution (*SFD*) and MFM hysteresis curves from an array of NWs presenting weak dipolar interaction

$$\frac{M^{MFM}(H)}{M_S^{MFM}} = \frac{N_{\text{up}} - N_{\text{down}}}{N_{\text{up}} + N_{\text{down}}} \tag{5.1}$$

where N_{up} and N_{down} stand to the number of NW in "up" and "down" states, respectively. Furthermore, the MFM-coercive field H_C^{MFM} is extracted from the image where the number of NWs (or NTs) with "up" and "down" states is same ($N_{\text{up}} = N_{\text{down}}$).

5 Review of MFM Results on Arrays of Magnetic NWs and NTs

5.1 Dense Arrays of Magnetic NWs

Electrodeposited magnetic NWs are an important member of the family of magnetic nanostructure. Several reports on studies of the magnetic properties of NWs by various techniques have been presented [3, 7, 8, 20, 21, 24, 41, 58–60 and the references therein]. These works presented in details the domain formation and the magnetization reversal mechanisms of various magnetic NWs such as Ni, Co, Fe, and their alloys and showed that domain formation is dependent on crystallinity and geometric parameters. The objective of this chapter is to cover only the MFM characterization of NWs arrays, therefore this section is devoted to the results obtained from NWs arrays deposited in polymer and alumina templates.

Although MFM has been used to explore the domain configuration of isolated NWs released from the templates in late 1990s [61], Asenjo et al. [29] presented MFM as a widely employed technique to observe the magnetic domains and walls in modern magnetic materials. Basics of domain formation, instrumentation and operation modes, interpretation of MFM results and representative images for thin films, magnetic data storage, amorphous and nanocrystalline alloys and nanowires have been described by the authors. Nielsch et al. [7] used alumina membrane to grow high-density, $\sim 10^{12}$ per cm^2, ordered porous arrays of Ni NWs using electrodeposition (Fig. 5.11a).

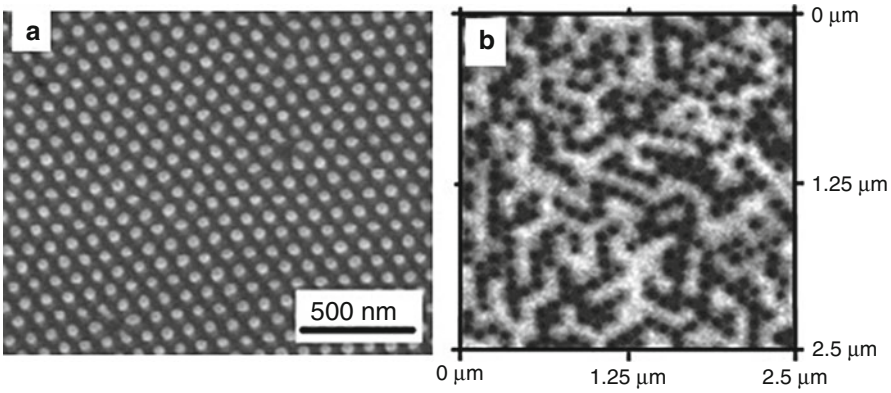

Fig. 5.11 Top view SEM micrograph of Ni filled alumina matrix (**a**) and MFM image of a demagnetized sample (**b**) showing the magnetization of the pillars "up" (*white*) and "down" (*black*). Reprinted with permission from [7]

The high coercivity and remanence in their system was attributed to the control of the NW diameter and ordered hexagonal arrangement. The MFM magnetic characterization, performed using a low-moment magnetic tip, agreed well with the bulk measurements. It was shown that switching of the individual single domain NWs, at various applied field after saturating the sample, was affected by the stray field generated by the nearest neighbors called demagnetizing field $H_D = \pi^2 M_s D^2 P \approx 550\ Oe$; *Ms* being the saturation magnetization, *D* is the diameter, and *P* is the pore density of the membrane. The labyrinth pattern of the domain structure in the demagnetized sample (Fig. 5.11b) was the result of the dipolar interactions. It was concluded that the stray field from the wires extended over several interwire distances due to their high aspect ratio.

The detailed comparison of the magnetic properties of different materials (Co, Fe, Ni, and Co-Pt) using different fabrication parameters identified the roles of magnetic anisotropy and magnetostatic interactions [41]. The authors illustrated schematically that the parallel alignment of two single domain neighbors in dense magnetic arrays is unfavorable as the dipolar field forces the orientation of the nearest neighbors (Fig. 5.12). Indeed, dipole-dipole interaction decreases with a power of 3 of the distance for an antiferromagnetic alignment.

Kou et al. were the first to suggest that dipolar interactions, which should be avoided to use NWs arrays as potential data storage candidate, can be used to induce an analog memory effect in magnetic NWs [62]. Based on this effect, they proposed an electromagnetic pulse (EMP) detection method using the NWs. EMP is generated by the nuclear or nonnuclear explosions and poses a serious threat to electronic devices by inducing a large current/voltage. Magnetic NWs record magnetic pulses passively. Once the magnetic component is recorded and read out, the electric component of the EMP can be calculated from the impedance of the propagating media.

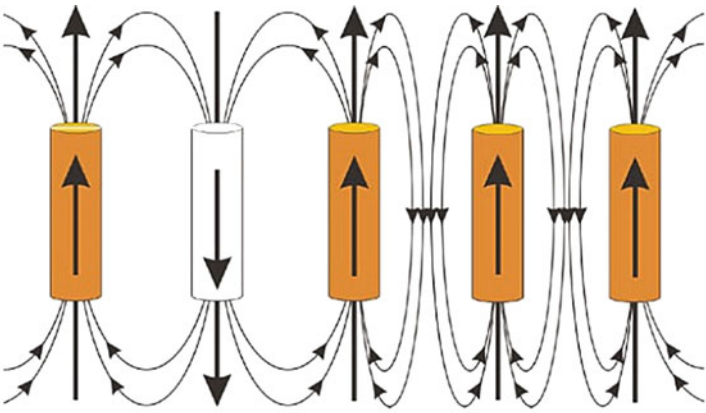

Fig. 5.12 Dipolar interactions illustrated on a cross-section of a nanowire array showing the energetically favored antiparallel orientation. Reprinted with permission from [41]

To understand the effect of stray fields of the neighboring wires which are the source of dipolar interactions, Sorop et al. [35] performed MFM measurements on single domain densely packed Fe NWs. They decomposed the macroscopic hysteresis curve into microscopic curves in terms of irreversible magnetic response of individual NWs using MFM. The single wires had always a square hysteresis whereas in the assembly of wires there was an asymmetry which found its natural explanation in the dipolar field generated by the neighboring wires. The average of interaction field coefficient measured from different single NWs was of the same order as the broadening/asymmetry of the macroscopic curves. It was concluded that the switching field of a wire will be different depending upon its magnetization orientation and the distance with the neighbors. This is true not only for the wires but also for other magnetic structures, e.g., nanodots [31, 63].

Using commercially available tips, the MFM contrast obtained on very dense Ni NWs arrays hardly allowed to distinguish NWs and to count the up and down wires (Fig. 5.13). Therefore, a method to extract the switching events and remanent magnetization by fitting the MFM data to Gaussian or Lorentzian distribution functions was proposed by Asenjo et al. [64]. Escrig et al. coupled numerical calculations and MFM analysis to obtain the information of magnetic remanence dependence of Ni NWs on their size [15]. Their model presented a way to calculate the remanence as a function of magnetic interactions in the NWs array. They also elaborated the importance of having a sufficient sample size for the reproducibility of MFM analysis.

In the above-mentioned examples, it was assumed that the total SFD is the result of the dipolar interactions [7, 35, 64]. It was needed to explore further that the broadening of the SFD was not only due to strong magnetic interactions in dense arrays but also due to geometrical parameters and fabrication flaws. The MFM study done by Wang et al. [8], to analyze the switching field of Co NWs one by one and removing the dipolar interaction field effects, established a base to extract intrinsic SFD of individual wires in interacting NWs. They investigated the magnetization

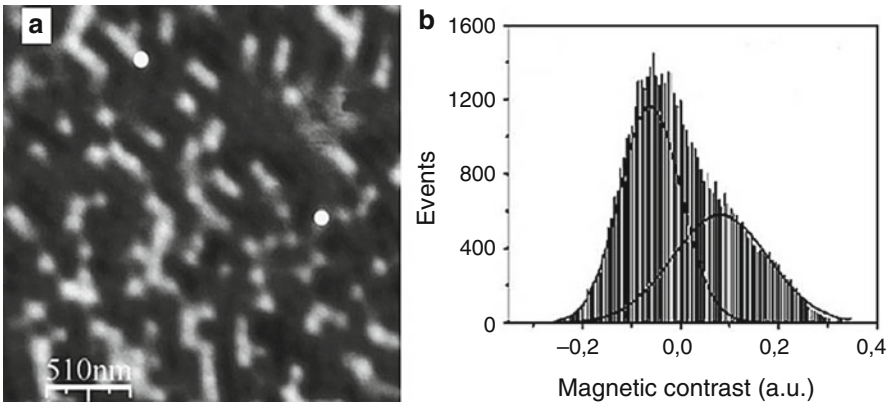

Fig. 5.13 MFM image showing NWs with magnetization up and down (**a**) and corresponding magnetic contrast distribution (**b**). Reprinted with permission from [64]

reversal progress of ordered Co NWs array by successive in-field MFM measurements. It was emphasized that in an assembly of magnetically saturated NWs, the field required to switch the first wire is the highest. It was suggested that the dipolar field H_{dip}, acting on a given nanorod at a random magnetization state might be expressed as

$$H_{\text{dip}} = x\frac{M}{M_s} \tag{5.2}$$

x representing the maximum dipolar field when the first rod switches in a saturated array. $\frac{M}{M_s}$ can be obtained by counting the number of reversed nanorods at each incremental step of applied field by applying Eq. 5.1 and its value is 1 when the NW array is saturated. By removing the dipolar field effect, calculated from Eq. 5.2, the intrinsic SFD can be obtained for the system under study. The intrinsic SFD extracted using this way was ~3 kOe. This value is quite significant and was attributed to geometric and compositional inhomogeneities along with the presence of dipolar interaction.

Yuan et al. [36] performed a similar work to calculate the dipolar field in an array of Co NWs (Fig. 5.14). They started applying the external fields with increments of 10 Oe from the AC erase state-base of the isothermal remanent magnetization IRM curve (IRM curve is obtained after the application and removal of an increasingly positive field with the sample initially demagnetized). They noted the field where the first switching event occurred. In a next step, measurements were started from the remanent state-top of DC demagnetizing DCD curve (DCD curve is obtained starting from the remanent state after saturating the sample) and negative incremental fields of 10 Oe were applied to record the same switching event. Average of these two fields gives the maximum dipolar field in the studied array. Subtracting this value from the total switching field gives the intrinsic SFD.

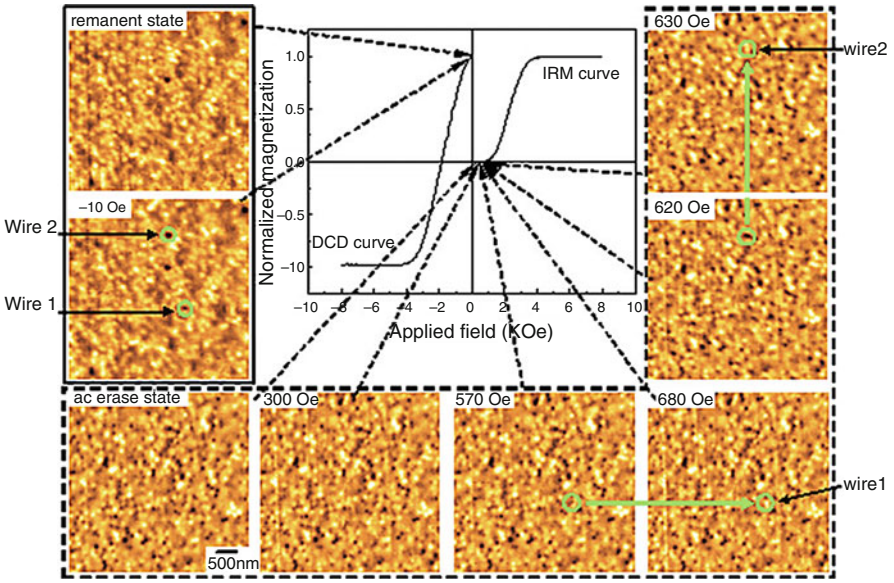

Fig. 5.14 Process for evaluating the dipolar field. Reprinted with permission from [36]

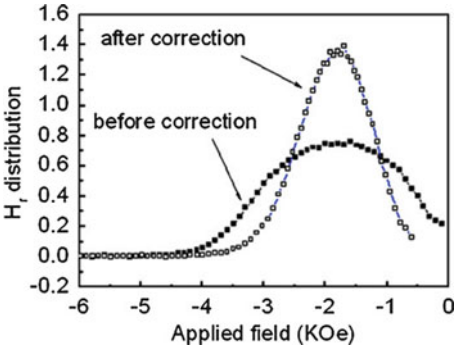

Fig. 5.15 Switching field distribution of the medium before and after magnetostatic field correction. Reprinted with permission from [36]

They also observed quite a large intrinsic SFD after removing the dipolar field (Fig. 5.15) and attributed it to diameter distribution, inhomogeneity of magnetic structures, and dispersion of interparticle separations [22, 23, 31, 63]. Numerical calculations were performed to exhibit the dependence of dipolar field on diameter and pitch of hexagonal NW array, and it was shown that the dipolar interactions effects decrease considerably by increasing the pitch and they are negligible at larger distances [24, 36, 41].

NTs present more degree of freedom to tune their magnetic properties as they possess a hollow core but they are still quite new in the family of magnetic nanostructures. This is the reason why they were not the subject of research from the MFM point of view. Nevertheless, the structural, magnetic, and magnetization

reversal properties of ferromagnetic NTs were investigated experimentally as a function of their geometrical parameters by other magnetometry techniques [9, 15, 25, 45, 46, 50, 65].

In multisegmented nanocylinders, with alternating magnetic wires and tubes segments, it was shown that the NT segments switch their magnetization before the NWs resulting in a trapped domain wall between the two segments [51]. This can be useful for encapsulating small magnetic particles inside such magnetic structures. These structures may also be used to perform logic functions.

It was shown that, thanks to their hollow structure, NTs present lower magnetic interactions compared with the same diameter and same density NWs [9, 45, 49]. It was further indicated that the physical reason of low exchange energy in NTs was the absence of curling related vortices which are present in other magnetic structures. The domain structure and the reversal mechanisms in NTs are strongly dependent upon their outer and inner diameters and the aspect ratios [40, 46, 53, 66–72]. This triggers the need of MFM characterization of the NTs as a function of their geometric parameters.

5.2 Dilute Arrays of NWs

The literature review presented herein made it clear that, in interacting arrays of magnetic NWs and NTs, the observed SFD is the sum of intrinsic parameter effect such as geometry, composition, etc., and of extrinsic parameter effects such as dipolar interactions [8, 35, 36]. Magnetic properties of NW arrays, in particular SFD and coercivity, were dependent on the degree of ordering, alloy composition, and the ratio of diameter and length to lattice parameter [22–24]. To use these magnetic nanostructures in novel devices, there is a basic need of understanding the magnetization reversal process and of controlling the SFD. As mentioned in the previous sections, efforts have been made to understand magnetization switching and to extract the intrinsic switching fields, from data on high-density NW arrays, by using certain corrective formulas. Experimental studies on isolated, noninteracting arrays of NWs/NTs to have an insight into their intrinsic properties have been rarely performed. Therefore, in the following section, our works based on MFM measurements on dilute arrays of NWs and NTs are presented. The objectives of these studies along with generating a model system for MFM in which we can apply in situ magnetic fields during the measurements were multi-fold and include:

(i) The determination of the magnetization reversal progress of noninteracting (i.e., absence of dipolar coupling) single domain ferromagnetic NWs arrays as synthesized using track-etch polymer template.
(ii) The determination of intrinsic switching field distribution (SFD) map.
(iii) The influence of geometrical parameters (like the diameter) on magnetic properties
(iv) The use and impact of different magnetic materials (Ni, $Ni_{1-x}Fe_x$, and $Co_{1-x}Fe_x$) to fabricate the NWs and NTs.

(v) The combination of MFM with bulk magnetometry technique (AGFM: Alternative Gradient Force Magnetometry) and with micromagnetic simulations to quantify the magnetic response from individual and from arrays of magnetic particles.
(vi) The effect of different morphologies (i.e., solid cylinders and hollow cylinders).

The experimental strategies to reach the above said goals have been presented in Sect. 2. The results in the subsequent section of this chapter will cover the outcomes of recent works. First of all, we cover the influence of diameter and materials and later we present the results of changing the morphology from NWs to NTs on the magnetization reversal process.

5.2.1 Effect of Material and Diameter on Intrinsic SFD

To fabricate and study low-density arrays of magnetic nanowires, polymer track-etched membranes were used as templates. Arrays of Ni and $Ni_{80}Fe_{20}$ and $Co_{55}Fe_{45}$ NWs have been fabricated by electrodeposition in low-packing-density (<1 %) nanoporous PC membranes. Such low porosity allowed neglecting the dipolar interaction. The length of the studied NWs, L, was equal to 4 ± 0.1 μm. Their diameter, D, was varied from 40 to 100 nm. The standard deviation on the diameter σ_D was equal to $\pm$ 5 nm. These parameters were determined by SEM analysis of the template membranes and of released NWs (Fig. 5.16).

The magnetic parameters of the materials (Ni, $Ni_{80}Fe_{20}$ and $Co_{55}Fe_{45}$) and the chosen range of D theoretically ensure single domain NWs. Indeed the domain wall width $\delta_{wall} = \pi\sqrt{A/K}$ (where A is the exchange stiffness and K is the magnetocrystalline anisotropy) for Ni is about 82 nm and even larger than 150 nm for $Ni_{80}Fe_{20}$. Consequently, for the nanowire samples considered in this study, only two remanent states are expected to be stable and correspond to a uniform magnetization aligned along + Oz and –Oz (+Oz being the NW's axis direction).

The low packing density of the arrays can be easily verified from different MFM images as it was illustrated in Fig. 5.5. Table 5.2 presents the template porosities P and the mean interwire distances of the first four neighboring NWs.

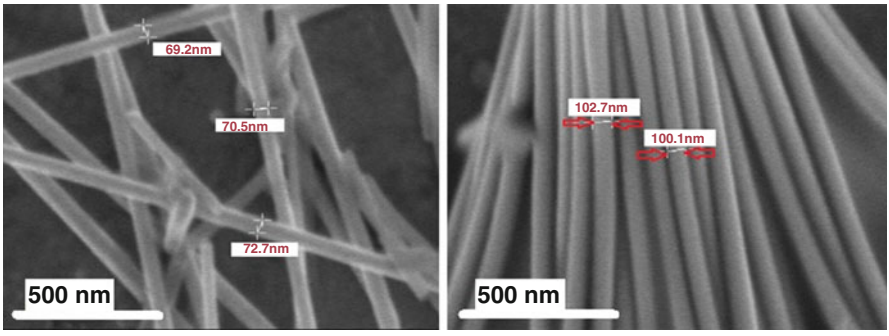

Fig. 5.16 SEM micrograph showing the diameter distribution of the Ni NWs for diameter 70 nm (*left*) and for diameter 100 nm (*right*)

Table 5.2 Template porosities "P" and the mean interwire distances

D (nm)	Measured P (%)	Interwire distance (nm)
40	0.04	~1200
50	0.15	~1000
70	0.19	~1000
100	0.24	~1200

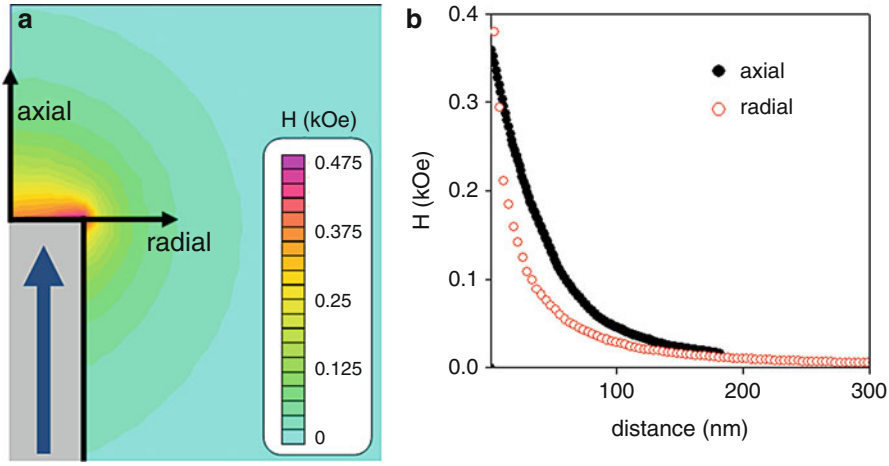

Fig. 5.17 Dipolar field emerging from a NiFe NW of diameter D = 100 nm uniformly magnetized ($4\pi M_S = 10$ kOe) calculated using FEMM (Meeker): (**a**) axial mapping of the field around the NW and (**b**) magnitude of the field along the NW axis and the radial axis. Reprinted with permission from [37]

It should be noted that the minimum interwire distance was rarely lower than around 600 nm which is large enough to hinder the presence of stray field interactions of the neighbors. Figure 5.17 shows the dipolar stray fields at the tip of a uniformly magnetized NW ($L = 4$ μm, $D = 100$ nm, $4\pi M_S = 10$ *kOe*) calculated using FEMM [73]. It illustrates that the dipolar field can be neglected in the present Ni and $Ni_{80}Fe_{20}$ and $Co_{55}Fe_{45}$ arrays since it is localized around the tip of the NWs and vanishes at 300 nm from the NW.

Figures 5.18, 5.19, and 5.20 present series of MFM images respectively obtained on an array of 50 nm $Ni_{80}Fe_{20}$ NWs, on an array of 70 nm $Co_{55}Fe_{45}$ NWs, and on 100 nm Ni NWs. The images were obtained at different remanent states. On the first images (top left of Figs. 5.18, 5.19, and 5.20), which corresponds to the one just after saturating the system, all the NWs are oriented in the same direction as revealed by the observation of only white spots.

Then, series of magnetic fields opposite to the sample initial saturation field were applied. The successive switching of the $Ni_{80}Fe_{20}$, $Co_{55}Fe_{45}$, and Ni NWs started around −500 Oe, −360 Oe, and −140 Oe till the application of −950 Oe, −1200 Oe, and −500 Oe, respectively, where all the NWs had been switched black.

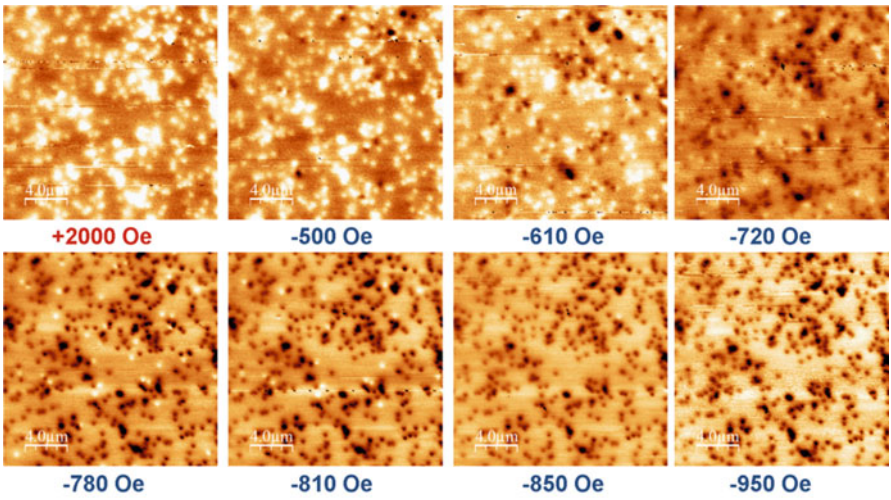

Fig. 5.18 Array of $Ni_{80}Fe_{20}$ NWs with $D = 50$ nm: series of MFM images (taken at zero applied field: see text) indicating the progress of magnetization reversal after saturation in a positive field (H = +2 kOe) and for different negative applied fields. Reprinted with permission from [37]

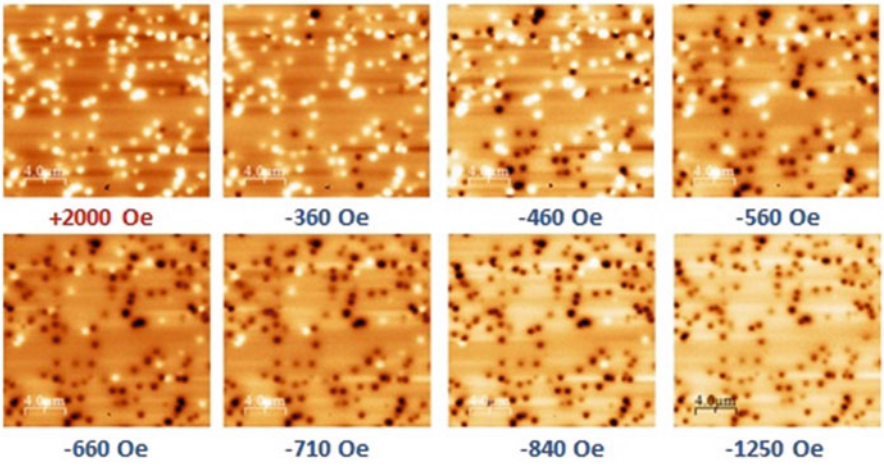

Fig. 5.19 MFM images of the $Co_{55}Fe_{45}$ nanowire array ($D = 70$ nm) at zero field after saturation in a positive 2 kOe field and then in a variety of nonsaturated remnant states obtained by changing each time the magnetic state of the nanowire array from saturation to a given negative field and then to remanence by reducing the field to zero. All the images were scanned in the same area

The spot sizes (black or white) are larger than the nominal diameters of the wires because MFM measures the dispersive stray field emanating from the wires and not the exact wire dimensions. From the images presented in Figs. 5.18, 5.19, and 5.20, we observed that the magnetization reversal of the array of NWs is nearly random

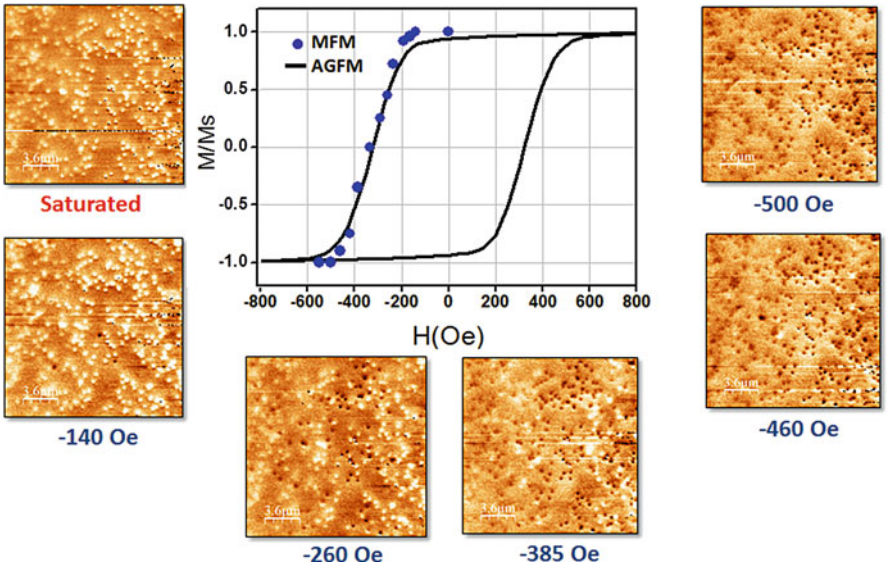

Fig. 5.20 Array of Ni NWs with $D = 100$ nm: series of MFM images (taken at zero applied field) indicating the progress of magnetization reversal after saturation in a positive field ($H = +2$ kOe) and for different negative applied fields

which supports the assumption of weak dipolar interactions. Indeed, in AAO arrays of NWs [7, 8, 23] exhibiting strong dipolar interactions, the switching of one NW was strongly influenced by the magnetization state of its neighbors.

The MFM magnetization curve of the 100 nm Ni NWs array has been obtained using Eq. 5.1 and showed a very nice match with the bulk AGFM cycle, plotted in Fig. 5.20. The MFM-magnetization curves obtained from the different Ni and $Ni_{80}Fe_{20}$ NW arrays (solid dots) are presented in Figs. 5.21a and 5.22a. The results from MFM and AGFM of $Ni_{80}Fe_{20}$ NWs arrays (continuous lines in Fig. 5.22a) were in good agreement and the same was true for Ni and $Co_{55}Fe_{45}$ NW arrays as well. The small deviations appearing between these two measurements can be attributed to the fact that a limited number of NWs are probed using MFM (local study) while the whole set of NWs is probed using magnetometry measurements.

The variation of H_C as a function of D for Ni and $Ni_{80}Fe_{20}$ NWs is presented in Figs. 5.21b and 5.22b. H_C increases with decreasing D. The same variation was observed for $Co_{55}Fe_{45}$ NWs arrays. For $Ni_{80}Fe_{20}$ NWs, it ranges from $H_C = 200$ Oe for $D = 100$ nm to $H_C = 800$ Oe for $D = 40$ nm and for Ni NWs from $H_C = 320$ Oe for $D = 100$ nm to $H_C = 650$ Oe for $D = 40$ nm. This dependence of H_C with diameter fits well with a D^{-2} law. It is well know that the H_C of an infinite NW, of certain diameter called critical diameter, in the coherent rotation model is given by $H_C = 2\pi M_S = 5$ kOe and does not depend on the diameter. Nevertheless, our NWs are not infinite and have diameters larger than $D_{coh} = 7.3 l_{ex} \approx 36$ nm (l_{ex} being the exchange length) which corresponds to the diameter beyond which non uniform reversal modes such as curling can occur [74].

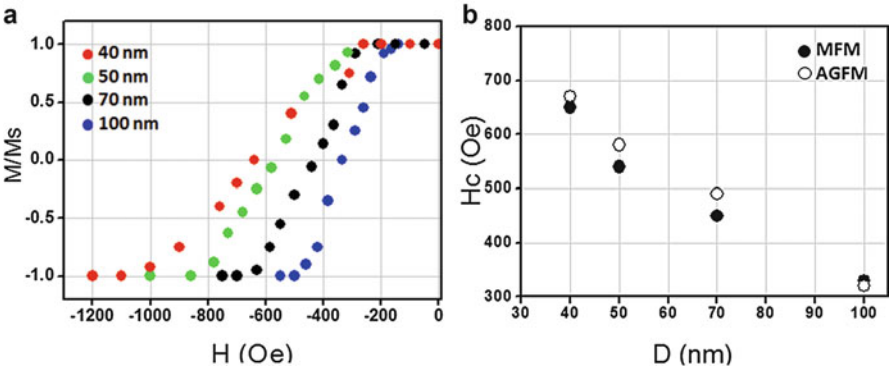

Fig. 5.21 (**a**) MFM-magnetization curves (*solid dots*) for the different arrays of Ni NWs. (**b**) Measured coercive field H_C as function of D

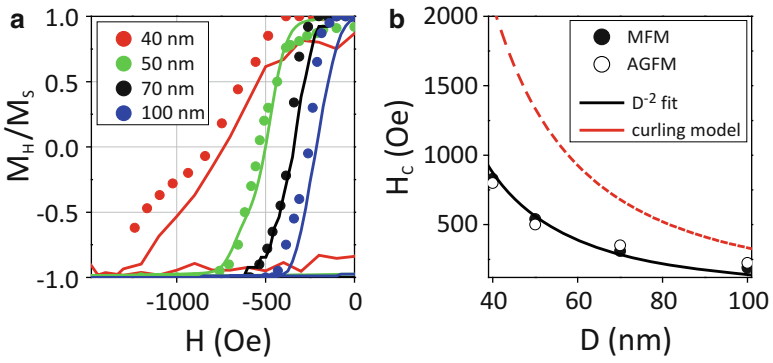

Fig. 5.22 (**a**) MFM-magnetization curves (*solid dots*) and bulk magnetization curves (*continuous lines*) for the different arrays of NWs. (**b**) Measured coercive field H_C as function of D (*empty* and *filled circles* form AGFM and MFM), *black continuous line* corresponds to a fit using a D^{-2} law while the *red dashed line* is obtained by using the analytical expression of H_C in the "curling model." Reprinted with permission from [37]

The D-dependence of H_C in the curling model has been calculated (see Fig. 5.22b) for infinite $Ni_{80}Fe_{20}$ NWs using the bulk magnetic parameter ($4\pi M_S = 10$ kOe and $A = 1 \times 10^{-6}$erg.cm^{-1}) [24, 74]. Although the measured H_C values are two times smaller than the ones found in the model, we observe the same D^{-2} dependence which shows that the reversal mechanism in these NWs resembles the curling model.

The SFD is linked to the number of switched NWs at each increment of the applied field and have been determined for $Ni_{80}Fe_{20}$ NWs arrays as a function of the applied fields; it is reported in Fig. 5.23a. The SFD width (δ_{SFD}) corresponds to the difference between the field of first reversed NW and the last one and is reported in Fig. 5.23b as a function of D. It decreases with increasing D, from 800 Oe for $D = 40$ nm to 320 Oe for $D = 100$ nm. The same trend was valid for Ni and

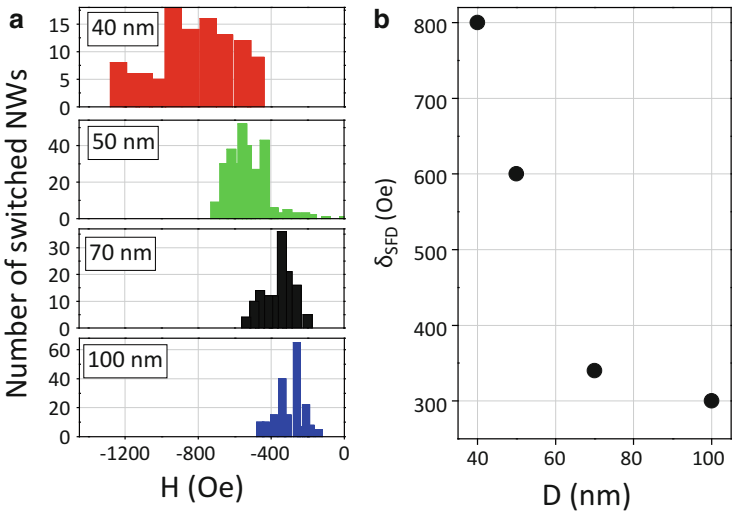

Fig. 5.23 (**a**) Switching field distributions of the different arrays of NiFe NWs. (**b**) Variation of the SFD width (δ_{SFD}) as a function of D

$Co_{55}Fe_{45}$ NWs as well. These values are smaller than the ones determined for densely packed NWs grown in alumina templates where δ_{SFD} was more than 2 kOe (for D around 40 nm) and where strong dipolar interactions were present [7, 35, 64]. It has been shown that the dipolar interactions in arrays of NWs with a fixed D and increasing P lead to a broadening of δ_{SFD} [75].

Let us assume that δ_{SFD} is defined as $\delta_{SFD} = \delta^D_{SFD} + \delta^0_{SFD}$ where, δ^D_{SFD} is due to the size distribution of D and δ^0_{SFD} may refer to the inhomogeneities in the structure and chemical composition of the NW arrays which also contribute to the broadening of the SFD. We propose to separately determine δ^D_{SFD} and δ^0_{SFD}. For this purpose, we consider a Gaussian size distribution of the NWs diameter with a standard deviation of ± 5 nm, as it agrees with the SEM measurements and we use the D^{-2} fit obtained from the experimental evolution of H_C with D (Fig. 5.22b).

Figure 5.24a presents the δ^D_{SFD} calculated by this way. It increases with decreasing D. The variation, of δ^D_{SFD} and H_C with D, are represented and fitted using D^{-2} laws in Fig. 5.24b. Note that δ^0_{SFD} is almost constant with D (empty square symbols in Fig. 5.24b). This proves that the increase of δ^D_{SFD} for smaller D is essentially due to the size distribution of the nanopores of the PC membrane while δ^0_{SFD} is due to other intrinsic effects.

5.3 Comparison of Dilute and Dense NW Arrays

In this section, the influence of dipolar interaction on the switching field distribution of arrays of NWs is discussed. Results from noninteracting arrays of NWs ($Ni_{80}Fe_{20}$

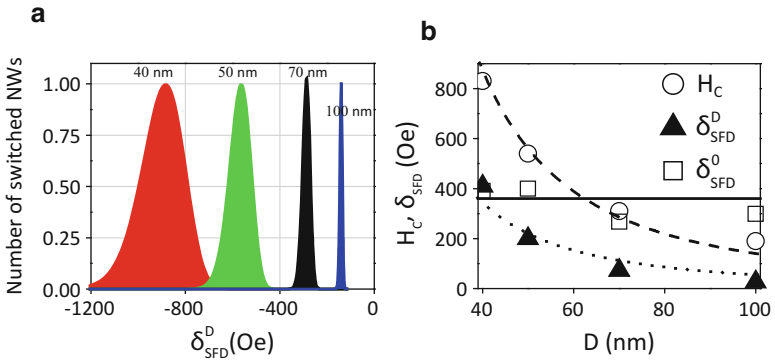

Fig. 5.24 (**a**) Calculated contribution of the size distribution of D (δ^D_{SFD}) obtained from the Gaussian size distribution of the polycarbonate nanopores and the D^{-2} fit of H_C. (**b**) Variation of H_C, δ^D_{SFD} and δ^0_{SFD} as a function of D. The *black* and *red continuous lines* are fits using D^{-2} law

and $Co_{55}Fe_{45}$) electrodeposited in low-packing-density PC membranes are compared to the ones coming from arrays of NWs electrodeposited into nanoporous AAO membranes. The noninteracting arrays have been electrodeposited in track-etched PC membranes of P less than 1 % and with pore diameters (D) ranging from 40 to100 nm. As mentioned in the previous section, the I_D between nanowires was found to be more than 600 nm which ensure that the role of the dipolar interaction between the NWs can be neglected. As a consequence, MFM images recorded in the remanent state and under an applied magnetic field were identical.

This is demonstrated by the MFM images of a $Co_{55}Fe_{45}$ nanowire array ($D = 50$ nm) in a positive 600 Oe field and as the field was lowered to zero (Fig. 5.25). It can be observed that both images are similar demonstrating that the low packing density of the NW array indeed leads to weak dipolar interactions between NWs and that measurement done at field H_0 and at zero applied field after applying field H_0 are same.

In addition, the demagnetized state of highly ordered and dense nanowire arrays in alumina template presents labyrinth domain pattern, as expected for a hexagonal pattern to maintain neighboring bits with antiparallel magnetization and to minimize the interwire dipolar field energy (Fig. 5.12). The demagnetized state of the present noninteracting arrays corresponds roughly 50 % of black (resp. white) spots, randomly distributed (Fig. 5.26) which is consistent with an array presenting negligible dipolar interactions.

Figure 5.27 presents the δ_{SFD} variation as function of D obtained from the noninteracting arrays of NWs ($Ni_{80}Fe_{20}$ and $Co_{55}Fe_{45}$). They are compared to the δ_{SFD} obtained from densely packed arrays of NWs electrodeposited into AAO membranes. These values are at least three times larger than the ones obtained for noninteracting arrays of NWs [37 and the references therein].

In the dense arrays, the dipolar interactions are strong and lead to a broadening of δ_{SFD}, whereas in low-packing-density arrays presented in the previous section,

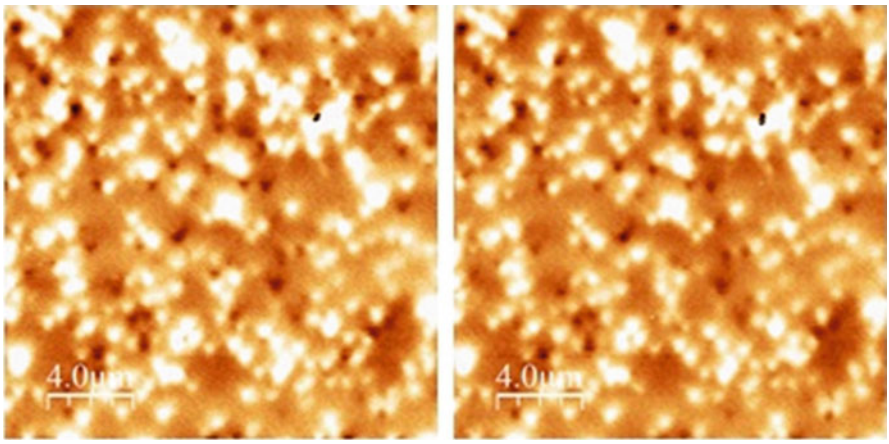

Fig. 5.25 MFM image of the $Co_{55}Fe_{45}$ nanowire array (D = 50 nm) in a positive 0.6 kOe field (*left*) and lowering the field to zero (*right*) to verify the noninteracting and bistable behavior of the nanowire array. Reprinted with permission from [37]

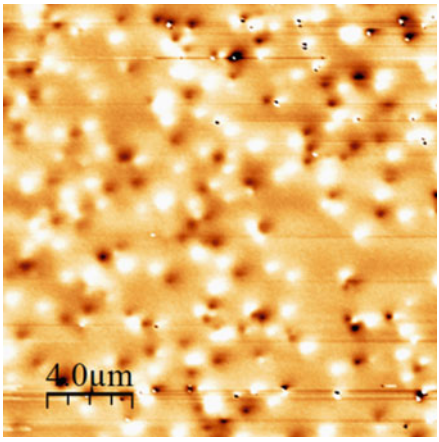

Fig. 5.26 MFM images of the AC-demagnetized $Co_{55}Fe_{45}$ nanowire array ($D = 100$ nm) of area $20 \times 20\ \mu m^2$

δ_{SFD} is essentially due to intrinsic effects and no complex calculations are required to discriminate between the intrinsic and dipolar contributions to the SFD. As already discussed in detail in Sect. 3.1, Yuan et al. and Wang et al. [7, 36] reported the intrinsic SFD in an array of Co NW ($D = 30$ nm) embedded in AAO membranes by evaluating and subtracting the total dipolar field present in the array. Even after subtracting the effect of this dipolar field, an intrinsic SFD width of about 4 kOe was estimated (i.e., about one order of magnitude larger than in the present study). The deviation of δ_{SFD} from an ideal Dirac function are due to parameters such as the distributions of diameter and length, the nonuniformity of the shape, inhomogeneities in the microstructure, and chemical composition of the NW.

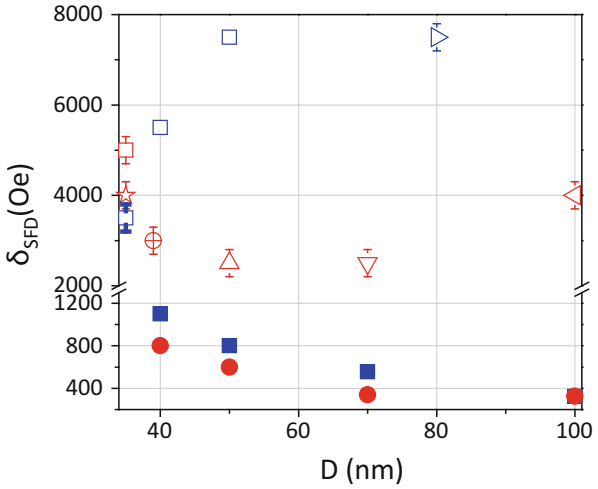

Fig. 5.27 Variation of δ_{SFD} of $Ni_{80}Fe_{20}$ (●) and $Co_{55}Fe_{45}$ (■) NW arrays as function of D and comparison with results obtained on NW arrays embedded in AAO templates; blue open symbols represent CoFe NWs whereas the red open symbols represent NiFe NW. Reprinted with permission from [37]

5.4 Nanowires Versus Nanotubes

After having discussed the effects of diameter and materials, one of the objectives is to present the magnetization reversal behavior of NTs and compare it with NWs. For this purpose, arrays of Ni NWs and NTs have been fabricated by electrodeposition in the same track-etched 21 μm thick PC membranes with pore diameter (D) of 150 ± 5 nm and pore density of 6 % [34]. By combining MFM and SEM images, the effective packing density in the NWs array is found to be $P_{NW} \sim 6$ %. The effective packing density in NTs array was $P_{NT} \sim 5$ % has to be calculated using the following equation:

$$P_{NT} = P_{NW}\left(1 - \beta^2\right) \tag{5.3}$$

where $\beta = r_1/r_2$ is the ratio of internal and external radii. P_{NT} was approximately equal to 5 %.

Figure 5.28a, b presents typical 10 × 10 μm^2 MFM images obtained at the top surface of the NW array and of the NT array, respectively. One would expect NTs to have a nonuniform MFM signal because of its hollow inner core. Nevertheless, from all the images, only "uniform" white or black spots are distinguishable as a function of the applied magnetic field. Subsequently, the arrays of NTs and NWs have been treated as apparent bistable system which is consistent with MFM scans and the already presented reports on Ni NWs [27].

Figure 5.29 presents a comparison between the bulk magnetization curves (obtained by AGFM) for the NT array (red continuous line) and for the NW array (blue dashed line). These magnetization curves clearly reveal that the NT curve is

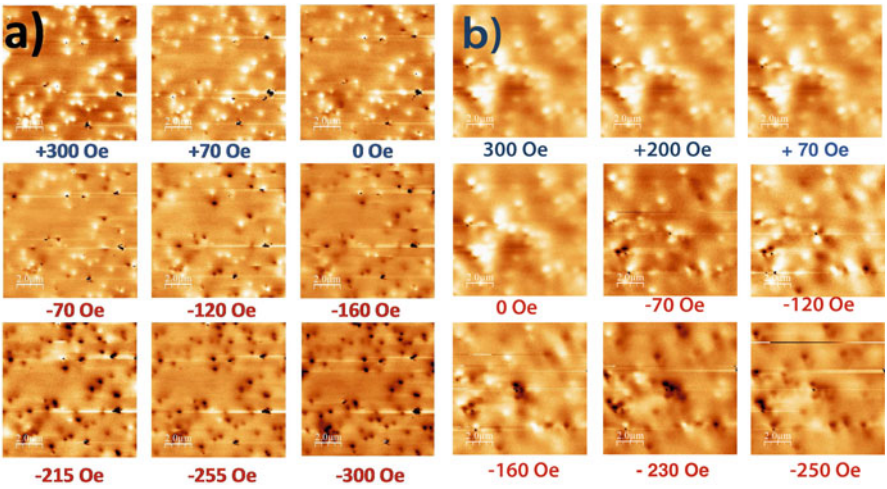

Fig. 5.28 In-field MFM images of Ni NWs (**a**) and NTs (**b**) starting at saturation in a positive 300 Oe field and at various negative magnetic fields displaying the magnetization reversal progress. The images are scanned at a fix area (10 × 10 μm^2)

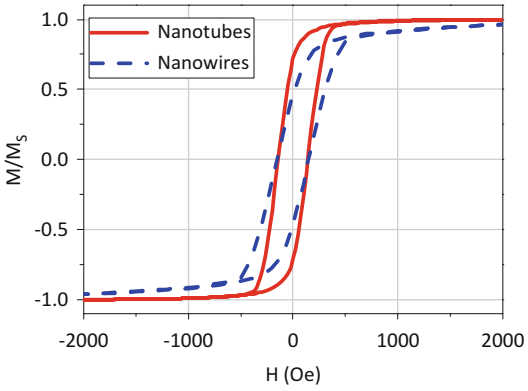

Fig. 5.29 Normalized AGFM magnetization curves obtained with a magnetic field aligned along the revolution axis from the arrays of NTs (*red solid line*) and NWs (*blue dashed line*). Reprinted with permission from [34], all rights reserved, © IOP Publishing

less tilted (more square) compared with the NW curve. The remanence of the NT array is about 0.8 while it is around 0.5 for the NW array. Moreover, the saturation field for the NWs is about two times higher (~2000 Oe) than for NTs (~1000 Oe). These observations are, in first approximation, coherent with the observations made by MFM where the NW reversal magnetization begins before and ends after the reversal of the NTs.

The difference of the two bulk magnetization curves may be understood solely in terms of the dipolar interactions and shape anisotropy contributions, since the magnetocrystalline anisotropy contribution in NWs and NTs may be neglected (this is due to the nontextured structure of the Ni) [21, 76, 77]. Considering that

the magnetization inside each NW and NT is uniform and because both NWs and NTs have the same symmetry with a large aspect ratio, the same mean field model used for NWs can be used for NTs, where the effective field H_{eff} in the saturated state is [54]:

$$H_{eff} = 2\pi M_S - 6\pi M_S P_{NW}\left(1 - \beta^2\right) \tag{5.4}$$

where M_s is the saturation magnetization for Ni and P_{NW} is the effective packing density of the considered array. The first term of this equation corresponds to the shape anisotropy contribution which is identical for both high-aspect-ratio NWs and NTs. The second term is the dipolar interactions contribution characterized by the effective packing density P_{NW} [78]. Due to their different volume, the packing fraction for NT (P_{NT}) is smaller than the NW (P_{NW}). It results in a weaker interaction field and thus a higher effective field and a strong uniaxial anisotropy for NTs. So, the key differences observed in the hysteresis loops arise from the respective effective fields and particularly from the dipolar interaction field. Moreover, the high packing value of the nanoporous template (6 %) results in stronger dipolar interaction and broader switching field distribution (SFD) [7, 23].

The MFM hysteresis curves were obtained by analyzing the MFM images presented in Fig. 5.28. From the MFM images, a remanence of 100 % was found in the case of NTs and around 80 % for the NWs while it reaches 80 and 50 % from the AGFM curves, respectively. Moreover, a saturation field of 300 Oe is deduced in both investigations for NTs while it was found to be around 1000 Oe for NWs arrays. Magnetometry and MFM hysteresis curves differ significantly, as presented in Fig. 5.30 for the array of NWs (a) and for the array of NTs (b) which was not the case for arrays of ferromagnetic NWs of diameter $\leq$ 100 nm (see Figs. 5.20 and 5.22a). In contrast, the coercive field values obtained from MFM and AGFM curves are the same.

From these comparisons, it can be deduced that the NWs and NTs present non uniform magnetization states. Indeed, the diameter of the studied NWs is around 150 nm which is far from the critical diameter below which a coherent rotation of the magnetization is expected for infinite Ni NW $D_{coh} = 7.3l_{ex} \approx 54$ nm [21] and nonuniform micromagnetic configurations may be present. Interestingly, from Fig. 5.30, it can be seen that the mismatch between bulk and MFM measurements is less pronounced in the curves for the NT array. This finding may be explained by the specific shape of the NTs compared to the NWs where the shell width is about 20 nm which prevents the presence of radial domains.

Therefore, from these findings, one can conclude that in both cases, the micromagnetic configuration is certainly non uniform. To reinforce this argument, micromagnetic simulations on an isolated NT and an isolated NW have been performed. The calculations have been performed using the NMAG package [79] and the results are presented in Fig. 5.31.

The dimensions used during simulations for the NW are length $L = 5$ µm and diameter $D = 150$ nm while for the NT $L = 5$ µm, outside diameter $D_{out} = 150$ nm, and inside diameter $D_{in} = 130$ nm. Note that these geometrical dimensions are close to the experimental ones. The magnetic parameters: magnetization saturation $M_S =$

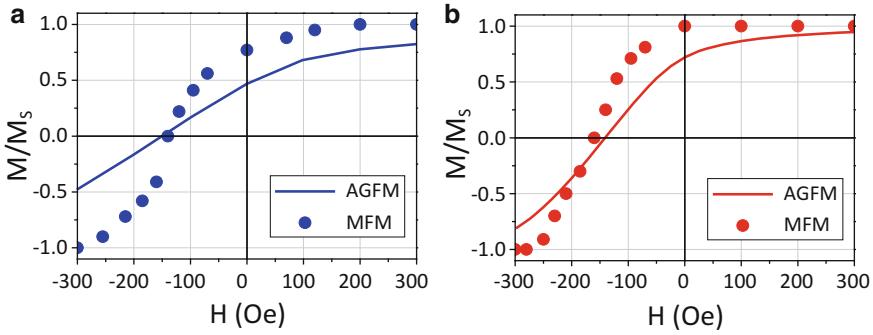

Fig. 5.30 Comparison of the in-field MFM magnetization curves with the ones obtained by AGFM measurements from the array of NWs (**a**) and NTs (**b**), respectively. Reprinted with permission from [34] all rights reserved, © IOP Publishing

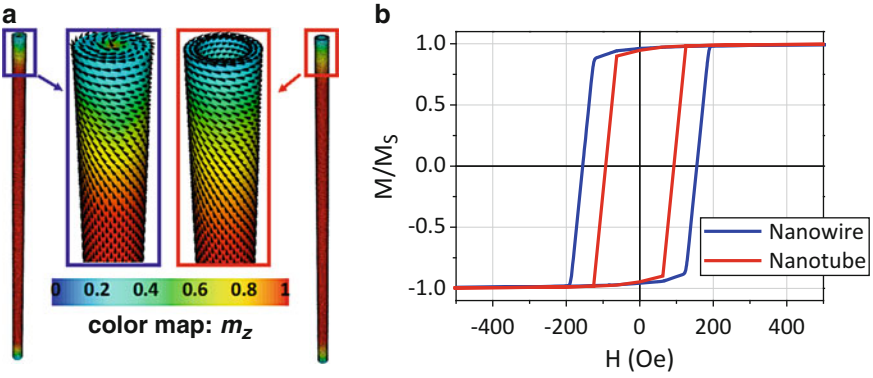

Fig. 5.31 (**a**) Magnetic moments distribution in an isolated NW and NT at zero applied field after applying a saturating field along the revolution axis. Colors encode m_z component of the magnetization (along the revolution axis). (**b**) Magnetization curves obtained for the isolated NW and the NT, respectively. Reprinted with permission from [34] all rights reserved, © IOP Publishing

0.48×10^3 emu.cm^{-3} and exchange stiffness $A = 1.0 \times 10^{-6}$ erg.cm^{-1} correspond to bulk values for Ni material which remain same for the NWs [76]. The magnetic moments distributions at remanence (after saturating the NW and the NT along the revolution axis) are presented in Fig. 5.31. It clearly depicts that the distribution at zero applied field is nonuniform in both cases. A quick overview of the already reported theoretical and experimental results further support the observations that the magnetic domains and magnetization reversal inside an infinite NW and a NT of larger diameters is not homogeneous [66, 67, 70, 80]. In this work, this is indirectly shown experimentally by combining the MFM and AGFM measurements. It is worth noting that contrary to the experimental hysteresis cycles (Fig. 5.29), the calculated hysteresis cycles (Fig. 5.31) are close to each other; the coercive field of the NT is slightly

weaker than the NW one. This strongly endorses that the main difference appearing between the experimental cycles is due to the higher dipolar interaction in NWs array.

The reasons why nanostructures of smaller dimensions are used to achieve the high-density storage media are twofold: first, to obtain a larger density and, second, to avoid inhomogeneous magnetic domains. The nanostructures used here have negligible intrinsic switching field distribution due to diameter distribution since they have larger diameters (see Sect. 3.2.1). The objective of using these dimensions in this work was to study the difference of reversal mechanisms and magnetic interactions in NWs and NTs. It is shown that even if the intrinsic SFD is not significantly modified, it is still slightly broader compared to lower-packing-density systems, especially for the NWs, due to stronger dipolar interactions and inhomogeneity of domains. For high-density systems, with smaller NT or NW diameter and low pitch, it is of prime importance to have a deep insight into not only magnetic interactions but also their intrinsic switching field which is strongly dependent upon the diameter distribution. The next step would be the study of systems with smaller diameters and reduced pitch where the present work will serve as a reference.

6 Conclusion and Future Works

This review has shown how MFM allows the characterization of arrays of magnetic NWs synthesized in nanoporous templates. The as fabricated NWs have high aspect ratio and negligible magnetocrystalline anisotropy; the magnetization is thus parallel to the NW axis and displays a bistable magnetic behavior. By analyzing the numbers of NWs with magnetization up and down, local magnetization curves are obtained.

The magnetic behavior of high-density arrays of magnetic NWs studied by various groups using MFM has been first reviewed. It has been shown that in the dense arrays of NWs, the switching behavior is largely affected by the dipolar interactions with nearest neighbors. Attempts were made to extract the intrinsic SFD from the measured one by theoretically evaluating the dipolar interaction contribution.

In order to directly measure the intrinsic contribution to the SFD, arrays of Ni, $Ni_{80}Fe_{20}$, and $Co_{55}Fe_{45}$ ferromagnetic NWs embedded into low-porosity nanoporous polycarbonate membranes has been systematically studied by in situ magnetic force microscopy. The MFM magnetization curves agreed well with the bulk magnetization measurements from AGFM. The images taken under continuous magnetic field and in the remanent state were compared and found to be identical demonstrating that for these low-density arrays the remanent state is identical to the in-field state due to the weak dipolar interaction.

The influence of the diameter on the magnetization reversal and the SFD was studied. Regardless of the NW diameter, narrow SFD were observed compared to the ones generally obtained for densely packed arrays in AAO membranes. Moreover, an increase of δ_{SFD} with decreasing diameter was observed and was qualitatively explained by considering the size distribution of the template nanopores and the diameter dependence of the NW coercive field. The magnetization reversal process

of Ni NWs and NTs arrays in PC template has also been investigated using MFM and AGFM. The comparison of the magnetization curves obtained with both techniques demonstrated that they are complementary. The mismatch between the magnetization curves in both cases suggested that the micromagnetic configurations inside the NWs and NTs are not coherent. Stronger dipolar interactions were observed in the NW array compared to the NT arrays.

The MFM results presented so far concerned arrays of NWs and NTs. However, MFM allows to observe the magnetic behavior of individual objects. It could thus be used to quantify experimentally the dipolar interaction field coefficient (IFC) between individual NWs and their neighbors as a function of the NW diameter and the average pitch of the magnetic array. This may be realized by measuring the magnetic fields necessary the switch down and back up the magnetic moment of individual NWs.

Acknowledgment M.R Tabasum is Assistant Professor on leave from department of industrial and manufacturing engineering RCET-UET Lahore. Financial support was provided by the Fédération Wallonie-Bruxelles (ARC 13/18-052 Supracryst) and by the Belgian Federal Science Policy (IAP-PAI 7/05). The authors thank the society it4ip (Louvain-la-Neuve, Belgium) for providing the polycarbonate track-etched membranes.

References

1. Alberto PG (2009) Principles of nanomagnetism. Springer, Berlin/Heidelberg
2. Encinas A, Vila L, Darques M, George JM, Piraux L (2007) Configurable multiband microwave absorption states prepared by field cycling in arrays of magnetic nanowires. Nanotechnology, 18:065705
3. Darques M, Spiegel J, De la Torre Medina J, Huynen I, Piraux L (2009) Ferromagnetic nanowire-loaded membranes for microwave electronics. J Magn Magn Mater 321:2055
4. Hamoir G, Piraux L, Huynen I (2013) Control of microwave circulation using unbiased ferromagnetic nanowires arrays. IEEE Trans Magn 49(7):4261
5. Favier F, Walter EC, Zach MP, Benter T, Penner RM (2001) Hydrogen sensors and switches from electrodeposited palladium mesowire arrays. Science 293:2227
6. Murray BJ, Walter EC, Penner RM (2004) Amine vapor sensing with silver mesowires. Nano Lett 4(4):665
7. Nielsch K, Wehrspohn RB, Fischer SF, Kronmiller H, Kirsehner J, Gosele U (2001) Magnetic properties of 100 nm-period nickel nanowire arrays obtained from ordered porous-alumina templates. Mater Res Soc Symp Proc 9:636
8. Wang T, Wang Y, Fu Y, Hasegawa T, Oshima H, Itoh K, Nishio K, Masuda H, Li FS, Saito H, Ishio S (2008) Magnetic behavior in an ordered Co nanorod array. Nanotechnology 19:455703
9. Proenca MP, Sousa CT, Escrig J, Ventura J, Vazquez M, Araujo JP (2013) Magnetic interactions and reversal mechanisms in Co nanowire and nanotube arrays. J Appl Phys 113:093907
10. Li J, Papadopoulos C, Xu JM (1999) Highly-ordered carbon nanotube arrays for electronics applications. Appl Phys Lett 75:367
11. Sun SH, Murray CB, Weller D, Folks L, Moser A (2000) Monodisperse FePt nanoparticles and ferromagnetic FePt nanocrystal superlattices. Science 287:1989
12. Martin CR, Baker LA (2005) Expanding the molecular electronics toolbox. Science 309:67
13. Martin CR, Kohli P (2003) The emerging field of nanotube biotechnology. Nat Rev Drug Discov 2:29

14. Lee SB, Mitchell DT, Trofin L, Nevanen TK, Soderlund H, Martin CR (2002) Antibody-based bio/nanotube membranes for enantiomeric drug separations. Science 296:2198
15. Escrig J, Altbir D, Jaafar M, Navas D, Asenjo A, Vázquez M (2007) Remanence of Ni nanowires: influence of size and labyrinth magnetic structure. Phys Rev B 75:184429
16. Lee J, Suess D, Schrefl T, Oh KH, Fidler J (2007) Magnetic characteristics of ferromagnetic nanotube. J Magn Magn Mater 310:2445
17. Choi D, Park J, Kim S, Gracias D, Cho M, Kim Y, Fung A, Lee S, Chen Y, Khanal S, Baral S, Kim J (2008) Hyperthermia with magnetic nanowires for inactivating living cells. J Nanosci Nanotechnol 8:1–5
18. Albrecht TT, Schotter TJ, Kästle CA, Emley N, Shibauchi T, Krusin-Elbaum L, Guarini K, Black CT, Tuominen MT, Russell TP (2000) Ultrahigh-density nanowire arrays grown in self-assembled diblock copolymer templates. Science 290:2126
19. Nicoleta L (2010) Electrodeposited nanowires and their applications. Intech-Olajnica, vol. 1, p 141
20. Fert A, Piraux L (1999) Magnetic nanowires. J Magn Magn Mater 200:338
21. Encinas-Oropesa A, Demand M, Piraux L, Huynen I, Ebels U (2001) Dipolar interactions in arrays of nickel nanowires studied by ferromagnetic resonance. Phys Rev B 63:104415
22. Vazquez M, Hernandez-Velez M, Pirota K, Asenjo A, Navas D, Velazquez J, Vargas P, Ramos C (2004) Arrays of Ni nanowires in alumina membranes: magnetic properties and spatial ordering. Eur Phys J B40:489
23. Navas D, Asenjo A, Jaafar M, Pirota KR, Hernandez-Velez M, Sanz R, Lee W, Nielsch K, Batallan F, Vazquez M (2005) Magnetic behavior of NixFe (100-x) ($65 < x < 100$) nanowire arrays. J Magn Magn Mater 290:191
24. Sun L, Hao Y, Chien CL, Searson PC (2005) Tuning the properties of magnetic nanowires. IBM J Res Dev 49:1
25. Han XF, Shamaila S, Sharif R, Chen JY, Liu HR, Dong-Ping L (2009) Structural and magnetic properties of various ferromagnetic nanotubes. Adv Mater 21:4619
26. Rosa WO, Jaafar M, Asenjo A, Vázquez M (2009) Co nanostructured array in patterned polymeric template. J Appl Phys 105:07C108
27. Sun L, Chen Q (2009) Core-shell cylindrical magnetic domains in Nickel nanowires prepared under magnetic flux. J Phys Chem C113:2710
28. Eftekhari A (2008) Nanostructured materials in electrochemistry. Wiley-VCH, Weinheim
29. Asenjo A, Garcia JM, Vazquez M (2001) Magnetic force microscopy: an advance technique for the observation of magnetic domains and walls. Recent Res Dev Magn 2:25
30. Jaafar M, Gomez-Herrero J, Gil A, Ares P, Vazquez M, Asenjo A (2009) Variable field magnetic force microscopy. Ultramicroscopy 109:693
31. Pei WL, Qin GW, Ren YP, Li S, Wang T, Hasegawa H, Ishio S, Yamane H (2011) Incoherent magnetization reversal in Co–Pt nanodots investigated by magnetic force microscopy. Acta Mater 59:4818
32. Jaafar M, Iglesias-Freire O, Serrano-Ramón L, Ibarra MR, de Teresa JM, Asenjo A (2011) Distinguishing magnetic and electrostatic interactions by a Kelvin probe force microscopy–-magnetic force microscopy combination. Beilstein J Nanotechnol 2:552
33. Piraux L, Antohe VA, Abreu Araujo F, Srivastava SK, Hehn M, Lacour D, Mangin S, Hauet T (2012) Periodic arrays of magnetic nanostructures by depositing Co/Pt multilayers on the barrier layer of ordered anodic alumina templates. Appl Phys Lett 101:013110
34. Tabasum MR, Zighem F, Medina JDLT, Encinas A, Piraux L, Nysten B (2014) Magnetic force microscopy investigation of arrays of nickel nanowires and nanotubes. Nanotechnology 25:245707
35. Sorop TG, Untiedt C, Luis F, Kröll M, Rasa M, de Jongh LJ (2003) Magnetization reversal of ferromagnetic nanowires studied by magnetic force microscopy. Phys Rev B 67:014402
36. Yuan J, Pei W, Hasagawa T, Washiyaa T, Saito H, Ishio S, Oshima H, Itoh K (2008) Study on magnetization reversal of cobalt nanowire arrays by magnetic force microscopy. J Magn Magn Mater 320:736

37. Tabasum MR, Zighem F, De La Torre Medina J, Piraux L, Nysten B (2013a) Intrinsic switching field distribution of arrays of $Ni_{80}Fe_{20}$ nanowires probed by in situ magnetic force microscopy. J Superconduct Novel Magn 26: 1375; Tabasum MR, Zighem F, Medina JDLT, Encinas A, Piraux L, Nysten B (2013b) Magnetic force microscopy study of the switching field distribution of low density arrays of single domain magnetic nanowires. J Appl Phys 113: 183908
38. Keller F, Hunter MS, Robinson DL (1953) Structural features of oxide coatings on aluminium. J Electrochem Soc 100(9):411
39. Masuda H, Fukuda K (1995) Ordered metal nanohole arrays made by a two-step replication of honeycomb structures of anodic alumina. Science 268:1466
40. Daub M, Knez M, Goesele U, Nielsch K (2007) Ferromagnetic nanotubes by atomic layer deposition in anodic alumina membranes. J Appl Phys 101:09J111
41. Schlorb H, Haehnel V, Khatri MS, Srivastav A, Kumar A, Schultz L, Fahler S (2010) Magnetic nanowires by electrodeposition within templates. Phys Status Solidi B 247(10):2364
42. Vater P (1988) Production and applications of nuclear track micro filter. Nucl Tracks Radiat Meas 15:743
43. Ferain E, Legras R (2003) Track-etch templates designed for micro- and nanofabrication. Nucl Instr Methods Phys Res B 208:115
44. Hu J, Odom TW, Lieber CM (1999) Chemistry and physics in one dimension: synthesis and properties of nanowires and nanotubes. Accounts Chem Res 32:435
45. Bao J, Tie C, Xu Z, Zhou Q, Shen D, Ma Q (2001) Template synthesis of an array of nickel nanotubules and its magnetic behavior. Adv Mater 13:21
46. Sui YC, Skomski R, Sorge KD, Sellmyer DJ (2004) Nanotube magnetism. Appl Phys Lett 84:1527
47. Wang Q, Wang G, Han X, Wang X, Hou JG (2005) Controllable template synthesis of Ni/Cu nanocable and Ni nanotube arrays: a one-step co-deposition and electrochemical etching method. J Phys Chem B 109:23326
48. Tao F, Guan M, Jiang Y, Zhu J, Xu Z, Xue Z (2006) An easy way to construct an ordered array of nickel nanotubes: the triblock-copolymer-assisted hard-template method. Adv Mater 18:2161
49. Liu J, Wang F, Zhai J, Ji J (2010) Controllable growth and magnetic characterization of electrodeposited nanocrystalline Ni-P alloy nanotube and nanowire arrays in AAO template. J Elect Chem 642:103
50. Rozman KZ, Pecko D, Suhodolcan L, McGuiness PJ, Kobe S (2011) Electrochemical syntheses of soft and hard magnetic $Fe_{50}Pd_{50}$-based nanotubes and their magnetic characterization. J Alloys Compd 509:551
51. Aravena DS, Corona RM, Goerlitz D, Nielsch K, Escrig J (2013) Magnetic properties of multisegmented cylindrical nanoparticles with alternating magnetic wire and tube segments. J Magn Magn Mater 346:171
52. Zhang HM, Zhang XL, Zhang JJ, Li ZY, Sun HY (2013) Fabrication and magnetic properties of CoNi alloy nanotube arrays. J Magn Magn Mater 342:69
53. Chen YH, Duan JL, Yao HJ, Mo D, Liu TQ, Wang TS, Hou MD, Sun YM, Liu J (2014) Facile preparation and magnetic properties of Ni nanotubes in polycarbonate ion-track templates. Phys B 441:1
54. Galvan YV, Martınez-Huerta JM, De La Torre Medina J, Danlee Y, Piraux L, Encinas A (2014) Dipolar interaction in arrays of magnetic nanotubes. J Phys Condens Matter 26:026001
55. Karim S, Maaz K (2011) Magnetic behavior of arrays of nickel nanowires: effect of microstructure and aspect ratio. Mat Chem Phys 130:1103
56. Hartmann U (1999) Magnetic force microscopy. Ann Rev Mater Sci 29:53
57. Ferri FA, Pereira-da-Silva MA, Marega EJ (2012) In: Bellitto V (ed) Magnetic force microscopy: basic principles and applications, atomic force microscopy – imaging, measuring and manipulating surfaces at the atomic scale. ISBN: 978-953-51-0414-8 InTech
58. Metzger RM, Konovalov VV, Sun M, Xu T, Zangari G, Xu B, Benakli M, Doyle WD (2000) Magnetic nanowires in hexagonally ordered pores of alumina. IEEE Trans Magn 36:30

59. McGary PD, Tan L, Zou J, Stadler BJH, Downey PR, Flatau AB (2006) Magnetic nanowires for acoustic sensors. J Appl Phys 99:08B310
60. Darques M, Piraux L, Encinas A, Bayle-Guillemaud P, Popa A, Ebels U (2005) Electrochemical control and selection of the structural and magnetic properties of cobalt nanowires. Appl Phys Lett 86:072508
61. Belliard L, Millat J, Thiaville A, Dubois S, Duvail JL, Piraux L (1998) Observing magnetic nanowires by means of magnetic force microscopy. J Magn Magn Mater 190:1
62. Kou X, Fan X, Dumas RK, Lu Q, Zhang Y, Zhu H, Zhang X, Liu K, Xiao JQ (2011) Memory effect in magnetic nanowire arrays. Adv Mater 23:1393
63. Chen YJ, Huang TL, Shi JZ, Deng J, Ding J, Li WM, Leong SH, Zong BY, Hnin Yu Yu Ko, Hu SB, Zhao JM (2012) Individual bit island reversal and switching field distribution in perpendicular magnetic bit patterned media. J Magn Magn Mater 324:264
64. Asenjo A, Jaafar M, Navas D, Vázquez M (2006) Quantitative magnetic force microscopy analysis of the magnetization process in nanowire arrays. J Appl Phys 100:023909
65. Sharif R, Shamaila S, Ma M, Yao LD, Yu RC, Han XF, Khaleeq-ur-Rahman M (2008) Magnetic switching of ferromagnetic nanotubes. Appl Phys Lett 92:032505
66. Chen AP, Gonzalez J, Guslienko KY (2012) Domain walls confined in magnetic nanotubes with uniaxial anisotropy. J Magn Magn Mater 324:3912
67. Lopez-Lopez JA, Cortés-Ortuno D, Landeros P (2012) Role of anisotropy on the domain wall properties of ferromagnetic nanotubes. J Magn Magn Mater 324:2024
68. Zhang Z, Zhang H, Wu T, Li Z, Zhang Z, Sun H (2013) Comparative study in fabrication and magnetic properties of FeNi alloy nanowires and nanotubes. J Magn Magn Mater 331:162
69. Wang XW, Yuan ZH, Fang BC (2011) Template-based synthesis and magnetic properties of Ni nanotube arrays with different diameters. Mater Chem Phys 125:1
70. Landeros P, Allende S, Escrig J, Salcedo E, Altbir D (2007) Reversal modes in magnetic nanotubes. Appl Phys Lett 90:102501
71. Usov NA, Zhukov A, Gonzalez J (2007) Domain walls and magnetization reversal process in soft magnetic nanowires and nanotubes. J Magn Magn Mater 316:255
72. Escrig J, Landeros P, Altbir D, Vogel EE, Vargas P (2007) Phase diagrams of magnetic nanotubes. J Magn Magn Mater 308:233
73. Meeker DC (2014) Finite element method magnetics (http://www.femm.info), used the package in
74. Aharoni A, Shtrikman S (1958) Magnetization curve of the infinite cylinder. Phys Rev 109:1522
75. Zighem F, Maurer T, Ott F, Chaboussant G (2011) Dipolar interactions in arrays of ferromagnetic nanowires: a micromagnetic study. J Appl Phys 109:013910
76. Ferré R, Ounadjela K, George JM, Piraux L, Dubois S (1997) Magnetization processes in nickel and cobalt electrodeposited nanowires. Phys Rev B 56:14066
77. Wang XW, Fei GT, Chen L, Xu XJ, Zhang LD (2007) Orientation-controllable growth of Ni nanowire arrays with different diameters. Electrochem Solid-State Lett 10(4):E1–E3
78. Nam B, Kim J, Hyeon JJ (2012) Analysis of effective permeability behaviors of magnetic hollow fibers filled in composite. J Appl Phys 111:07E347
79. Fischbacher T, Franchin M, Bordignon G, Fangohr H (2007) A systematic approach to multiphysics extensions of finite-element-based micromagnetic simulations: NMAG. IEEE Trans Magn 43:2896
80. Rozman KZ, Rhein F, Wolff U, Neu V (2014) Single-vortex magnetization distribution and its reversal behaviour in Co-Pt nanotubes. Acta Mater 81:469